Journal of Japan Association for Earthquake Engineering, Vol. 19, No. 3, 2019

EFFECTS OF DIFFERENT WAYS OF COUNTING FAULT AREA FOR ASPERITY MODEL OF CRUSTAL EARTHQUAKES ON FAULT PARAMETERS AND PREDICTED STRONG GROUND MOTIONS

Masanobu TOHDO[1], Atsuko OANA[2] and Kazuo DAN[3]

[1] Member, Ohsaki Research Institute, Inc., Dr. Eng.
Tokyo, Japan, tohdo@ohsaki.co.jp
[2] Member, Institute of Technology, Shimizu Corporation, Dr. Eng.
Tokyo, Japan, a.oana@shimz.co.jp
[3] Member, Ohsaki Research Institute, Inc., Dr. Eng.
Tokyo, Japan, dan@ohsaki.co.jp

ABSTRACT: The effects of two different ways of counting fault areas, that are the seismic fault area and the entire ruptured fault area, on the strong ground motions from the faults 30 km and 50 km long were small for peak ground accelerations and comparatively large for peak ground velocities and response spectra in the longer period range. On the other hand, the effects on the strong ground motions from the fault 200 km long were little for peak ground accelerations or peak ground velocities while the effects were a little for response spectra in the period range longer than 3 seconds.

Key Words: Crustal earthquake, Strong ground motion prediction, Recipe, Asperity model, Counting way of fault area, Fault parameter

1. INTRODUCTION

The asperity model is adopted in the official procedure of evaluating fault parameters, so called Recipe, by the Headquarters for Earthquake Research Promotion (2016)[1)] for strong motion prediction, and it has been commonly used in Japan. This Recipe describes the procedure of evaluating fault parameters for each type of earthquakes: crustal earthquakes, subduction plate-boundary earthquakes, and intra-slab earthquakes. And empirical relationships among fault parameters play an important role for all these three types of earthquakes.

In the empirical relationships for evaluating the seismic moment, shown later by equations (3) to (5) in Chapter 2, the area S_{seis} of the seismic fault located in the seismogenic layer is taken as the fault area. However, many of the fault areas in the reference data include shallow parts of the faults over the seismogenic layer *i.e.* the fault ruptured area S.

Hence, in this paper, we distinguished the seismic fault area S_{seis} and the entire fault ruptured area S, and examined the effects of the different ways of counting fault area, S_{seis} or S, on the outer and inner fault parameters and the calculated strong motions.

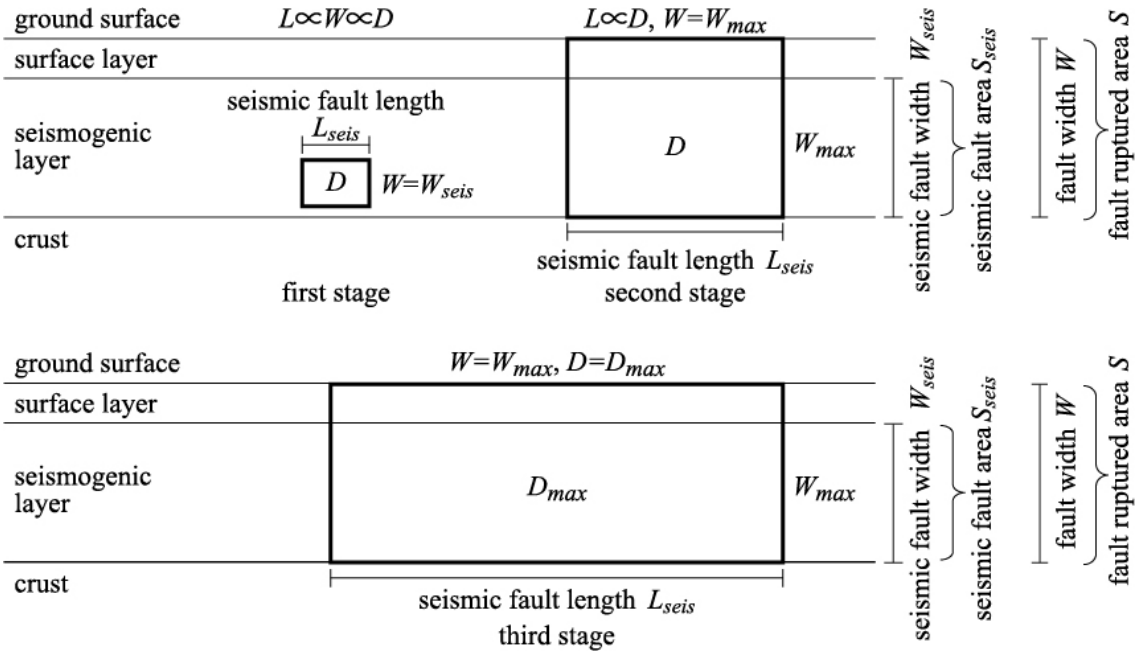

Fig. 1 Image of the ruptured fault and the seismic fault (three-stage model)

2. SCALING LAW OF THE OUTER FAULT PARAMETERS OF THE EARTHQUAKES CAUSED BY ACTIVE FAULTS AND THE RECIPE

2.1 Scaling law of the outer fault parameters

The empirical scaling law between the seismic moment and the fault area is often described by the three-stage model (*e.g.* Irikura and Miyake, 2011)[2]. In the first stage of this three-stage model, the fault length, width, and averaged slip are proportional to each other, and the seismic moment is proportional to the 1.5 square of the fault area. In the second stage, the fault width saturates because of the thickness of the seismogenic layer, the fault length and slip are proportional to each other, and the seismic moment is proportional to the 2 square of the fault area. In the third stage, the averaged slip also saturates, and the seismic moment is proportional to the fault area. Figure 1 shows the image of the fault at each stage. This three-stage model is adopted for crustal earthquakes in the Recipe by the Headquartes of Earthquake Research Promotion (2016)[1].

2.2 Evaluation procedure of fault parameters of the asperity model in the Recipe

Major parameters describing the asperity model are the seismic fault area S_{seis}, the averaged stress drop $\Delta\sigma$, the asperity area S_{asp}, the asperity stress drop $\Delta\sigma_{asp}$, the seismic moment M_0, and the short-period level A. Here, the short-period level is the flat level of the acceleration source spectrum in the short-period range (Dan *et al*., 2001)[3]. Since these major parameters are related by three relationships shown later by equations (7) to (9), all the six major parameters can be determined when three of them are given.

In the Recipe by the Headquarters for Earthquake Research Promotion (2016)[1], the seismic fault area S_{seis} is determined by the following equation (1) from the length of the seismic fault L_{seis} and the width W_{seis}, shown in Fig. 1:

$$S_{seis} = L_{seis} W_{seis}. \tag{1}$$

The seismic fault width W_{seis} in the second and third stages is calculated by

$$W_{seis} = (dep2 - dep1) / \sin\delta. \tag{2}$$

Here, $dep1$ is the upper depth of the seismogenic layer, $dep2$ is the lower depth of the seismogenic layer, and δ is the dip angle of the fault.

Next, the seismic moment is evaluated by one of the following equations (3) to (5):

$$M_0[\mathrm{N\cdot m}] = \left(\frac{S_{seis}[\mathrm{km}^2]}{2.23\times10^{-15}}\right)^{3/2}\times10^{-7} \quad \text{for} \quad M_0 < 7.5\times10^{18}\ \mathrm{N\cdot m}, \tag{3}$$

$$M_0[\mathrm{N\cdot m}] = \left(\frac{S_{seis}[\mathrm{km}^2]}{4.24\times10^{-11}}\right)^{2}\times10^{-7} \quad \text{for} \quad 7.5\times10^{18}\ \mathrm{N\cdot m} \leqq M_0 \leqq 1.8\times10^{20}\ \mathrm{N\cdot m}, \tag{4}$$

$$M_0[\mathrm{N\cdot m}] = S_{seis}[\mathrm{km}^2]\times10^{17} \quad \text{for} \quad 1.8\times10^{20}\ \mathrm{N\cdot m} < M_0. \tag{5}$$

Equation (3) was proposed by Somerville *et al.* (1999)[4], equation (4) by Irikura and Miyake (2001)[5], and equation (5) by Murotani *et al*. (2015)[6]. The short-period level is evaluated by the following equation (6) of Dan *et al*. (2001)[3] from the seismic moment:

$$A[\mathrm{N\cdot m/s}^2] = 2.46\times10^{10}\times(M_0[\mathrm{N\cdot m}]\times10^7)^{1/3}. \tag{6}$$

On the other hand, the six major parameters are related by the following relationships:

$$\Delta\sigma = \frac{7}{16}\frac{M_0}{(S_{seis}/\pi)^{3/2}}, \tag{7}$$

$$S_{seis}\Delta\sigma = S_{asp}\Delta\sigma_{asp}, \tag{8}$$

$$A = 4\pi\beta_{seis}^2\sqrt{\frac{S_{asp}}{\pi}}\Delta\sigma_{asp}. \tag{9}$$

Here, β_{seis} is the *S*-wave velocity at the source.

Equation (7) is a theoretical relationship between the seismic fault area S_{seis}, the seismic moment M_0, and the averaged stress drop $\Delta\sigma$ in the circular crack model by Eshelby (1957)[7]. Equation (8) is a general equation about an asperity model by Madariaga (1979)[8]. Equation (9) is an empirical equation by Brune (1970)[9] for the circular crack model, and it is expanded to the asperity model by Boatwright (1988)[10] after examination of the dynamic fault rupturing simulation. Equation (9) neglects the short-period level of the motions generated on the background, which is much smaller than that on the asperity.

The averaged stress drop $\Delta\sigma$, the asperity area S_{asp}, and the stress drop on the asperity $\Delta\sigma_{asp}$ are calculated by equations (7) to (9) by using S_{seis}, M_0, and A. We have to note here that when the fault length gets longer, the asperity area S_{asp} calculated by equations (7) to (9) becomes over 50% of the area of the seismic fault S_{seis} and then the slip on the background D_{back} becomes negative because the slip on the asperity D_{asp} is calculated by the following equation of Somerville *et al*. (1999)[4]:

$$D_{asp} = 2D_{seis}. \tag{10}$$

Here, D_{seis} is the averaged slip on the seismic fault, and it is calculated by

$$D_{seis} = M_0 / (\mu_{seis} S_{seis}). \tag{11}$$

where μ_{seis} is the rigidity at the source.

In order to avoid the negative slip on the background, the Headquarters for Earthquake Research Promotion (2016)[1] suggest to adopt 14.4 MPa as the stress drop on the asperities $\Delta\sigma_{asp}$ and 3.1 MPa as the averaged stress drop $\Delta\sigma$ all over the seismic fault by Fujii and Matsu'ura (2000)[11]:

$$\Delta\sigma_{asp} = 14.4 \text{ MPa}, \tag{12}$$

$$\Delta\sigma = 3.1 \text{ MPa}. \tag{13}$$

In this case, the ratio of the area of the asperities to that of the seismic fault is calculated as follows from equation (8):

$$S_{asp} / S_{seis} = \Delta\sigma / \Delta\sigma_{asp} = 0.215. \tag{14}$$

Hereafter, we refer to the method by using equation (7) as a method of circular crack equation and to the method by using equations (12) and (13) as a tentative method. Note here that the Recipe describes that the tentative method is always applied to the third-stage earthquakes.

3. DIFFERENCE OF COUNTING THE FAULT AREA AND ITS EFFECTS ON OTHER PARAMETERS

The Recipe describes the empirical relationship between the seismic moment M_0 and the seismic fault area S_{seis} proposed by Irikura and Miyake (2001)[5] for the second-stage earthquakes. However, the fault area of the 1992 Landers, California, earthquake is not only the seismic fault area but also the shallow part of the fault *i.e*. the entire ruptured fault area, which is shown as an example in Irikura and Miyake (2001)[5].

Irikura *et al*. (2017)[12] recently showed that the relationship between the fault area and seismic moment of the 2016 Kumamoto, Japan, earthquake agreed with the empirical relationship by Irikura and Miyake (2001)[5], and they adopted the entire fault ruptured area, including the shallow part of the fault, as the fault area. Moreover, Irikura and Miyake (2001)[5] used the database by Wells and Coppersmith (1994)[13] to obtain equation (4), and the fault width is the entire fault width W when the rupture reaches the ground surface (Wells, 2016, Personal Communication).

Similarily, the database by Murotani *et al*. (2015)[6] used to obtain equation (5) includes no fault from which they trimmed out the shallow part (Murotani, 2016, Personal Communication).

Different ways of counting the fault area in equations (4) or (5), *i.e*. the seismic fault area S_{seis} by equation (1) described in the Recipe or the fault ruptured area S by equation (15) based on the database, lead to the different seismic moments, and then different short-period levels.

$$S = L_{seis} W \tag{15}$$

Hence, we examined the effects of the different ways of counting the fault area on the fault parameters and on the resultant strong motions. In this paper, the fault model by the seismic fault area S_{seis} is designated S_{seis} model (seismic- fault-area model), and the fault model by the entire fault rupture area S is designated S model (entire fault-rupture-area model).

Table 1 Evaluation equations of the fault parameters for the second-stage earthquakes by the method of circular crack equation and effects of different ways of counting the fault area on the fault parameters

parameters		equation	ratio of the S model to the S_{seis} model
outer fault parameters	seismic fault area	$S_{seis} = L_{seis}W_{seis}$ or $S = L_{seis}W$	(W/W_{seis})
	seismic moment	$M_0[\mathrm{N\cdot m}] = \left(\frac{S_{seis} \text{ or } S[\mathrm{km}^2]}{4.24\times10^{-11}}\right)^2 \times 10^{-7}$	$(W/W_{seis})^2$
	short-period level	$A[\mathrm{N\cdot m/s^2}] = 2.46\times10^{10} \times (M_0[\mathrm{N\cdot m}]\times10^7)^{1/3}$	$(W/W_{seis})^{2/3}$
	averaged stress drop	$\Delta\sigma = \frac{7}{16}\frac{M_0}{(S_{seis}/\pi)^{3/2}}$	$(W/W_{seis})^2$
	averaged slip	$D_{seis} = \frac{M_0}{\mu_{seis}S_{seis}}$	$(W/W_{seis})^2$
inner fault parameters	asperity area ratio	$\frac{S_{asp}}{S_{seis}} = \left(\frac{4\sqrt{\pi S_{seis}}\Delta\sigma\beta_{seis}^2}{A}\right)^2$	$(W/W_{seis})^{8/3}$
	asperity stress drop	$\Delta\sigma_{asp} = \Delta\sigma / \left(\frac{S_{asp}}{S_{seis}}\right)$	$(W/W_{seis})^{-2/3}$
	asperity slip	$D_{asp} = 2D_{seis}$	$(W/W_{seis})^2$

We examined the effects of the choice of the S_{seis} model or S model on each evaluated fault parameter. Table 1 lists the effects for the second-stage earthquakes. These are the results by the method of circular crack equation. Here, we assumed that the entire seismic moment M_0 was assigned to the deep part of the fault (seismic fault) because the stress drop occurs on the deep part of the fault, not on the shallow part, and then the slip on the shallow part is induced by the slip on the deep part (Dalguer *et al*., 2001)[14] and because the rigidity of the soil in the shallow part is smaller than that in the deep part and then most of the seismic moment is released on the deep part (Irie *et al*., 2010)[15]. Detailed explanation is in Appendix.

Therefore, even for the S model, we used S_{seis} to evaluate the averaged stress drop $\Delta\sigma$, the averaged slip D_{seis}, the asperity area ratio S_{asp}/S_{seis}, and the asperity stress drop $\Delta\sigma_{asp}$.

Table 1 shows that, for the same fault length, the difference of the seismic moment M_0 is $(W/W_{seis})^2$, and the difference of the ratio of the asperity area to the seismic fault area S_{asp}/S_{seis} is $(W/W_{seis})^{8/3}$. Meanwhile, the difference of the asperity stress drop $\Delta\sigma_{asp}$ is $(W/W_{seis})^{-2/3}$.

For example, when *dep*1 is 3 km and *dep*2 is 18 km, the difference of the seismic fault area is $W/W_{seis} = (18/\sin\delta)/(15/\sin\delta) = 1.2$, the difference of the seismic moment is $1.2^2 = 1.44$, and the difference of the ratio of the asperity area to the seismic fault area is $1.2^{8/3} = 1.63$. The difference of the asperity stress drop is $1.2^{-2/3} = 0.89$.

Table 2 lists the effects for the third-stage earthquakes. These are the results by the tentative method. Here, as well as the second-stage earthquakes, we assumed again that all the seismic moment was assigned to the deep part of the fault (seismic fault) where the stress drop occurred. We adopted 14.4 MPa as the asperity stress drop both in the S_{seis} model and the S model, according to the Recipe.

Table 2 Evaluation equations of the fault parameters for the third-stage earthquakes by the tentative method and effects of different ways of counting the fault area on the fault parameters

parameter		equation	ratio of the S model to the S_{seis} model
outer fault parameters	seismic fault area	$S_{seis} = L_{seis}W_{seis}$ or $S = L_{seis}W$	(W/W_{seis})
	seismic moment	$M_0[\mathrm{N\cdot m}] = (S_{seis}$ or $S\,[\mathrm{km}^2]) \times 10^{-7}$	(W/W_{seis})
	averaged slip	$D_{seis} = \dfrac{M_0}{\mu_{seis}S_{seis}}$	(W/W_{seis})
inner fault parameters	asperity area	$S_{asp} = S_{seis} \times (\Delta\sigma / \Delta\sigma_{asp}) = 0.215S_{seis}$	1
	asperity stress drop	$\Delta\sigma_{asp} = 14.4\,\mathrm{MPa}$	1
	asperity slip	$D_{asp} = 2D_{seis}$	(W/W_{seis})
short-period level		$A = 4\pi\beta_{seis}^2\sqrt{\dfrac{S_{asp}}{\pi}}\Delta\sigma_{asp}$	1

Table 2 shows that, for the same fault length, the difference of the seismic moment M_0 is (W/W_{seis}). For example, when *dep*1 is 3 km and *dep*2 is 18 km, the difference of the seismic moment is $W/W_{seis} = (18/\sin\delta)/(15/\sin\delta) = 1.2$. Meanwhile, the asperity area, the asperity stress drop, and the short-period level are not changed.

4. EXAMPLES OF FAULT MODELS AND CALCULATION OF STRONG MOTIONS

4.1 Making fault models

In order to examine the effect of the choice of the S_{seis} model or S model on the synthesized strong motions, we made two vertical left-lateral strike-slip faults with the length of 30 km and 50 km in the second stage and one vertical left-lateral strike-slip fault with the length of 200 km in the third stage. Here, we selected representative fault lengths considering that the boundary of the second stage and the third stage is the fault length of about 80 to 100 km. The upper depth of the seismogenic layer was assumed to be 3 km and the lower depth to be 18 km for the three faults. The 50-km long fault was assumed to consist of a 30-km long segment and a 20-km long segment, and the 200-km long fault was assumed to consist of eight 25-km long segments. We evaluated the parameters of each fault by the two methods of the S_{seis} model and the S model. Here, as mentioned in Chapter 3, we assumed that no strong motions were generated in the shallow part of the fault located in the surface layer because the shallow part has no stress drop, moves with the movement of the deep part of the fault, and the rigidity of the shallow part is smaller than that of the deep part. We assumed the density to be $\rho_{seis} = 2.7$ g/cm^3 and the *S*-wave velocity to be $\beta_{sei\,s} = 3.46$ km/s at the source.

Table 3 Parameters of the faults with the lengths of 30 km, 50 km and 200 km for simulating strong motions

parameter \ model			30-km length		50-km length		200-km length	
			S_{seis} model	S model	S_{seis} model	S model	S_{seis} model	S model
fault length L, upper and lower depth of the seismogenic layer $dep\,1$, $dep\,2$		km	L=30, $dep\,1$=3, $dep\,2$=18		L=50, $dep\,1$=3, $dep\,2$=18		L=200, $dep\,1$=3, $dep\,2$=18	
fault ruptured area S, seismic fault area S_{seis}		km^2	S=540, S_{seis}=450		S=900, S_{seis}=750		S=3600, S_{seis}=3000	
seismic moment M_0		N·m	1.13E+19	1.62E+19	3.13E+19	4.51E+19	3.00E+20	3.60E+20
moment magnitude M_W		-	6.6	6.7	6.9	7.0	7.6	7.6
averaged slip D_{seis}		m	0.8	1.1	1.3	1.9	3.1	3.7
averaged stress drop $\Delta\sigma$		MPa	2.9	4.1	3.7	5.3	3.1	3.1
short-period level A		$N\cdot m/s^2$	1.19E+19	1.34E+19	1.67E+19	1.89E+19	3.11E+19	3.11E+19
asperity	area ratio S_{asp}/S_{seis}	-	0.19	0.31	0.27	0.43	0.215	0.215
	slip D_{asp}	m	1.5	2.2	2.6	3.7	6.2	7.4
	stress drop $\Delta\sigma_{asp}$	MPa	15.1	13.4	13.9	12.3	14.4	14.4

Table 3 lists the fault parameters, and Figure 2 shows asperity models of the S_{seis} model and the S model for simulating strong motions.

According to the Recipe, we assigned one or two asperities to one segment, and the ratio of the asperity areas was assumed to be 16:6 (Somerville *et al*., 1999)[4] when the segment had two asperities. We located the asperities almost in the center along the depth, and set the upper depth of the asperity in the S_{seis} model and that in the S model to be the same. We located the hypocenter 1 at the left bottom corner of the larger asperity and the hypocenter 2 at the right bottom corner of the smaller asperity, according to the Recipe. We adopted the radial rupture propagation and the rupture propagation velocity of 2.49 km/s *i.e.* $0.72\beta_{seis}$ (Geller, 1976)[16], according to the Recipe.

4.2 Calculation of strong motions by the stochastic Green's function method

We adopted the stochastic Green's function method by Dan *et al*. (2010)[17], generating the *SH*- and *SV*-waves from each subfault, to calculate the strong motions. Here, the radiation pattern was the theoretical value (Aki and Richards, 1980)[18] in the frequency range lower than 3 Hz, the averaged value of 0.445 (Boore and Boatwright, 1984)[19] in the frequency range higher than 6 Hz, and the logarithmically interpolated value between the theoretical value and the averaged value in the frequency range of 3 to 6 Hz, according to Satoh (2002)[20]. Here, the sign of 0.445 was taken from the sign of the theoretical value. We assumed the f_{max} to be 6 Hz (Tsurugi *et al*., 1997)[21] and the quality factor to be $Q(f) = 100f$ for 0.8 Hz or higher and $Q(f) = 80$ for 0.8 Hz or lower. We evaluated the soil amplification by the impedance ratio between the seismogenic layer (density ρ_{seis} = 2.7 g/cm^2, *S*-wave velocity β_{seis} = 3.46 km/s) and the bed rock (density ρ_{engb} = 1.9 g/cm^3, *S*-wave velocity β_{engb} = 0.5 km/s). Figure 3 shows the soil profile used in the calculation of the strong motions by the stochastic Green's function method.

Note here that the ground motions in the frequency range lower than 3 Hz calculated by the stochastic Green's function method are based on the far-field *S*-wave solution for the point source (Aki

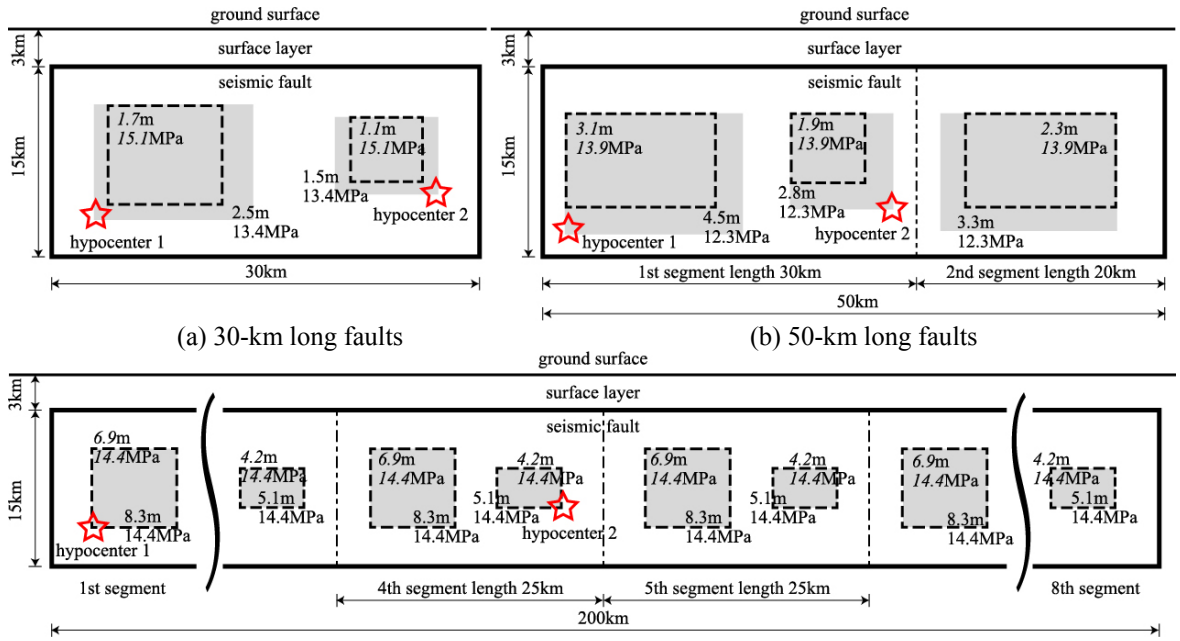

(a) 30-km long faults (b) 50-km long faults

(c) 200-km long faults

Fig.2 Asperity models of the S_{seis} model and the S model for simulating strong motions. The gray parts are the asperities, and the asperities shown by the broken lines are for the S_{seis} model. The upper values are the slips on the asperities D_{asp} and the lower values are the asperity stress drops $\Delta\sigma_{asp}$. The italic numbers are for the S_{seis} model. The stars named as the hypocenter are the rupture starting points.

and Richards, 1980)[18] and that this far-field *S*-wave solution is not sufficient in low frequencies at a calculation point of the shortest distance from the fault of 3 km. Therefore, we examined the limitation of our calculation by the theoretical result of Nozu (2006)[22]. Nozu (2006)[22] showed the ratio of the summation of *N* (near-field term), *IP* (intermediate-field *P*-wave term), *IS* (intermediate-field *S*-wave term), and *FS* (far-field *S*-wave term) to *FS* as follows:

$$(N+IP+IS+FS)/FS = 6i\cdot\{1-\exp[-in\cdot(\eta-1)]\}/n^3 - 6\{1-\eta\cdot\exp[-in\cdot(\eta-1)]\}/n^2 + 2i\cdot\eta^2\cdot\exp[-in\cdot(\eta-1)]/n - 3i/n + 1 \quad (16)$$

Here, $i=\sqrt{-1}$, $n=\omega r/\beta$, $\eta=\beta/\alpha=1/3^{0.5}$, ω is the circular frequency, r is the distance from the source, β is the *S*-wave velocity, and α is the *P*-wave velocity. When we take r = 3 km and β = 3.46 km/s, ω = 0.27 rad/s if we choose 1.5 of equation (16) as a criterion of underestimation of the calculated motions. Consequently, ground motions in the period range longer than 23 seconds might be underestimated 70% in our calculations.

As for the size of the sub-fault, we took 1 km × 1 km for the 30-km long fault and 2 km×1.875 km for the 50-km and 200-km long faults by considering the difference of the asperity areas. The number of the calculation points are 297, 341, and 228 for the fault length of 30 km, 50 km, and 200 km, respectively. We distributed the calculation points at every 5-km grid on the line projection on the ground surface of the fault and in the one-side area within 50 km from it due to the symmetry of the fault model, except at 10-km grids between 30 to 50 km from the line projection in the case of the 200-km long fault. All the calculation points are on the surface of the engineering bed rock.

4.2.1 Examples of the velocity motions and Fourier spectra

Figure 4 shows examples of the calculated velocity motions by the S_{seis} model and the S model at the

engineering bed rock	density	ρ_{engb}
	S-wave velocity	β_{engb}
transition layer	density	$\rho = \sqrt{\rho_{seis}\rho_{engb}}$
	S-wave velocity	$\beta = \sqrt{\beta_{seis}\beta_{engb}}$
seismogenic layer	density	ρ_{seis}
	S-wave velocity	β_{seis}

Fig. 3 Soil profile for the stochastic Green's function method.

right edge, center, and left edge of the line projection of the fault with the length of 30 km on the ground surface. We observe pulses in the calculated motions at the center of the line projection, and the amplitude of the pulse by the S model is 1.1 times the amplitude by the S_{seis} model. This is because the span of the rupture propagation on the asperity in the S model is longer than that in the S_{seis} model (Miyatake, 1998)[23].

Figure 5 shows the root mean square of the Fourier spectra of the two horizontal components at the center of the line projection of the faults on the ground surface. The difference is not clear in the high-frequency range between the Fourier spectrum by S_{seis} model and that by the S model, which variate largely, and the Fourier spectrum by the S model is larger than that by the S_{seis} model in the low-frequency range. The difference of the Fourier spectra in the low-frequency range corresponds to the ratio of 1.4 between the asperity slip of 2.5 m in the S model and that of 1.7 m in the S_{seis} model for the 30-km long faults. Similarly, the difference corresponds to the ratio of 4.5 m/3.1 m = 1.4 for the 50-km long faults and to the ratio of 8.3 m/6.9 m = 1.2 for the 200-km long faults.

The following peak ground accelerations and the peak ground velocities are the maximum amplitude from the origin to the orbit plotted by the fault parallel component and fault normal component of the calculated motion at each point. The response spectra are also the maximum amplitude from the origin to the orbit.

4.2.2 Peak ground accelerations PGA's

Figure 6 compares the PGA's by the S_{seis} model with those by the S model. Figure 6(a) shows that ratios of the PGA's by the S model to those by the S_{seis} model are 0.9 to 1.2 and 1 in average in the case of the 30-km long fault. Figure 6(b) shows the ratios of the PGA's by the S model to those by the S_{seis} model are 0.9 to 1.1 at many points and 1 in average in the case of the 50-km long fault. The PGA's by the S model are not difference so much from those by the S_{seis} model. This is because the asperity area S_{asp} in the S model is larger than that in the S_{seis} model while the asperity stress drop in the S_{seis} model is larger than that in the S model.

Figure 6(c) shows that the PGA by the S_{seis} model is almost the same as that by the S model at every calculation point in the case of the 200-km long faults. This is because the asperity area S_{asp} in the S_{seis} model is the same as that in the S model and the asperity stress drop $\Delta\sigma_{asp}$ in the S_{seis} model is the same as that in the S model.

On the other hand, the PGA's from the 30-km long faults with the hypocenter 1 exceed 1,000 cm/s^2 at some points both in the S_{seis} model and the S model, while those with the hypocenter 2 exceed 1,000 cm/s at no points. In order to examine the effects by the difference of the hypocenter, Figure 7 shows the distribution of the PGA's by the S_{seis} model and the S model for the 30-km long faults. The red points, indicating the PGA over 1000 cm/s^2, are observed in the right side of the hypocenter 1 both in the S_{seis} model and the S model, while no red points are observed in the case of the hypocenter 2. The reason why we observe the red points, indicating the PGA over 1000 cm/s^2, only in the case of the hypocenter 1 is that the span of the rupture propagation from the hypocenter 1 to the upper right side in the larger asperity is longer than that from the hypocenter 2 to the upper left side in the smaller asperity (Miyatake, 1998)[23].

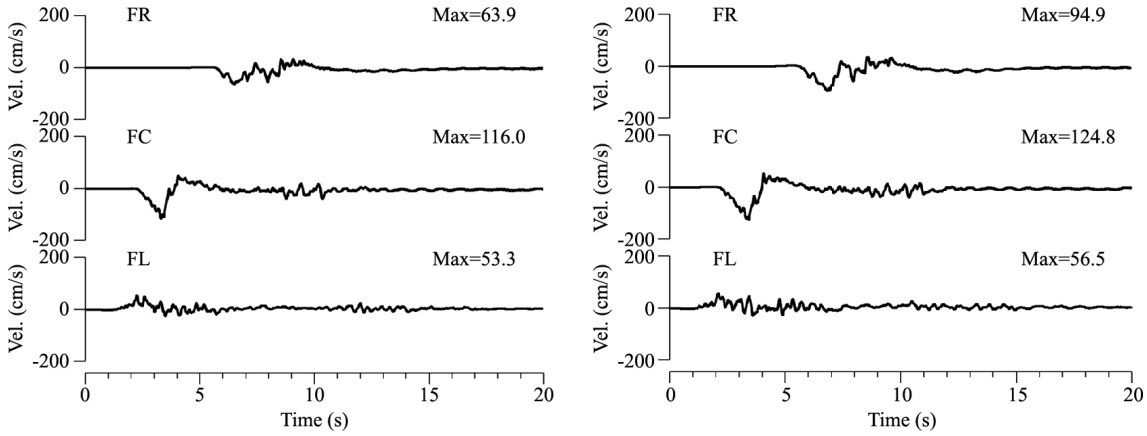

Fig. 4 Examples of the velocity motions of the fault normal component at the right edge of the projection of the fault on the ground surface (FR), the center (FC), and the left edge (FL) in the case of the 30-km long fault with the hypocenter 1.

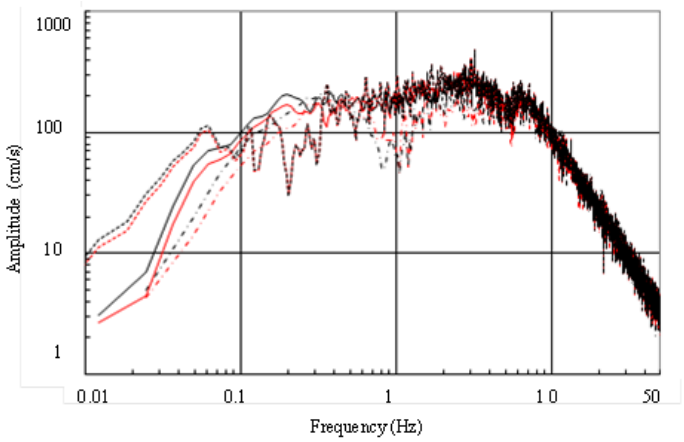

Fig. 5 Fourier spectra of the motions at the center of the line projection of the faults on the ground surface. The red lines are for the S_{seis} model, the black for the S model, the broken lines for the fault of the length of 30 km, the solid lines for that of the length of 50 km, and the dotted lines for that of the length of 200 km.

4.2.3 Peak ground velocities PGV's

Figure 8 compares the PGV's by the S_{seis} model and those by the S model. Figure 8(a) shows the PGV's for the 30-km long faults, and the ratios of the PGV's by the S model to those by the S_{seis} model are 0.9 to 1.4, indicating the PGV by the S model is larger than that by the S_{seis} model at many calculation points. Figure 8(b) shows the PGV's for the 50-km long faults, and it is found that the ratios of the PGV's by the S model to those by the S_{seis} model are 0.9 to 1.4 and that the PGV's by the S model are larger than those by the S_{seis} model at many calculation points. The reason why the PGV's by the S model are larger than those by the S_{seis} model for the second-stage earthquakes is that the short-period level of the S model is 1.13 times larger than that of the S_{seis} model and the asperity slip D_{asp} in the S model is 1.44 times larger than that in the S_{seis} model.

Figure 8(c) shows the PGV's for the 200-km long faults, and it is found out that the PGV's by the S_{seis} model are almost the same as those by the S model, as the PGA's. This is because the asperity area and the asperity stress drop are common in both of the models, while the asperity slips are different.

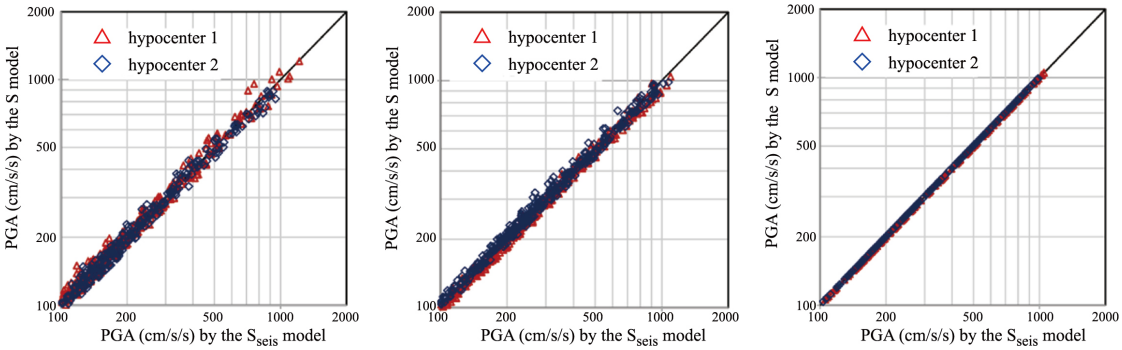

(a) 30-km long faults (b) 50-km long faults (c) 200-km long faults

Fig. 6 Comparison of the PGA's by the S_{seis} model with those by the S model.

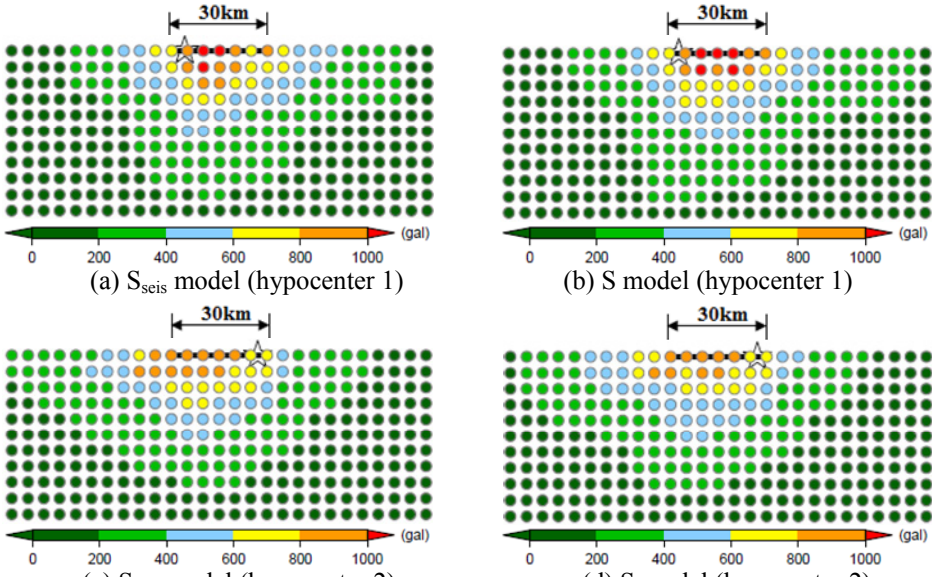

(a) S_{seis} model (hypocenter 1) (b) S model (hypocenter 1)

(c) S_{seis} model (hypocenter 2) (d) S model (hypocenter 2)

Fig. 7 Distribution of the PGA's by the S_{seis} model and the S model for the 30-km long faults. The black line is the projection of the fault model on the ground surface, and the star is the projection of the hypocenter.

The PGV's from the 30-km long faults with the hypocenter 1, shown in Fig. 8(a), exceed 100 cm/s at some points both in the S_{seis} model and the S model, while those with the hypocenter 2 exceed 100 cm/s at no points. Also, the PGV's from the 50-km long faults with the hypocenter 1, shown in Fig. 8(b), exceed 125 cm/s at some points both in the S_{seis} model and the S model.

In order to examine the difference of the results by the difference of the locations of the hypocenters, we show the PGV distributions by the S_{seis} model and by the S model for 30-km long faults in Fig. 9. Figures 9(a) and 9(b) show that the red points indicating PGV's over 100 cm/s appear just above the faults on the right side of the hypocenter 1 both in the S_{seis} model and the S model. On the other hand, Figures 9(c) and 9(d) show that no red points indicating PGV's over 100 cm/s are observed. Similarly, we show the PGV distributions by the S_{seis} model and the S model for 50-km long faults in Fig. 10. The PGV's over 125 cm/s are observed at points just above the left segment on the right side of the hypocenter 1 both in the S_{seis} model and the S model. The reason why we observe the red points, indicating the PGV over 100 cm/s of the 30-km long fault and that over 125 cm/s of the 50-km long fault in the case of the hypocenter 1 is that the span of the rupture propagation from the hypocenter 1 to the upper right side in the larger asperity is longer than that from the hypocenter 2 to the upper left side in the smaller asperity (Miyatake, 1998)[23].

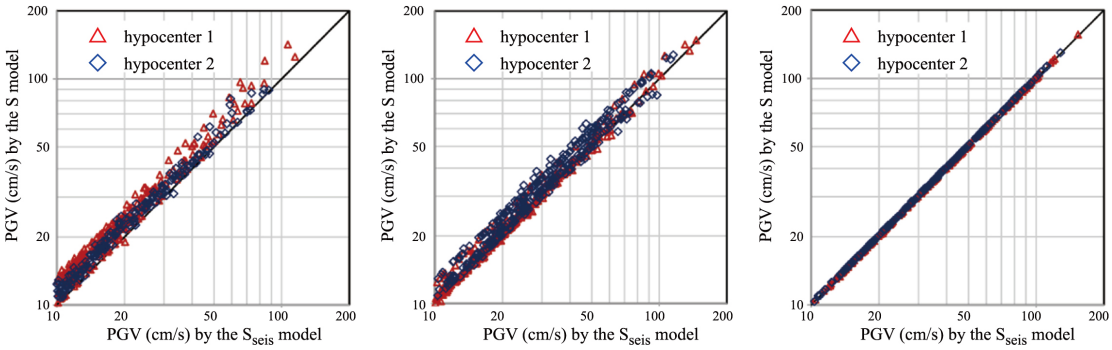

(a) 30-km long faults (b) 50-km long faults (c) 200-km long faults

Fig. 8 Comparison of the PGV's by the S_{seis} model with those by the S model.

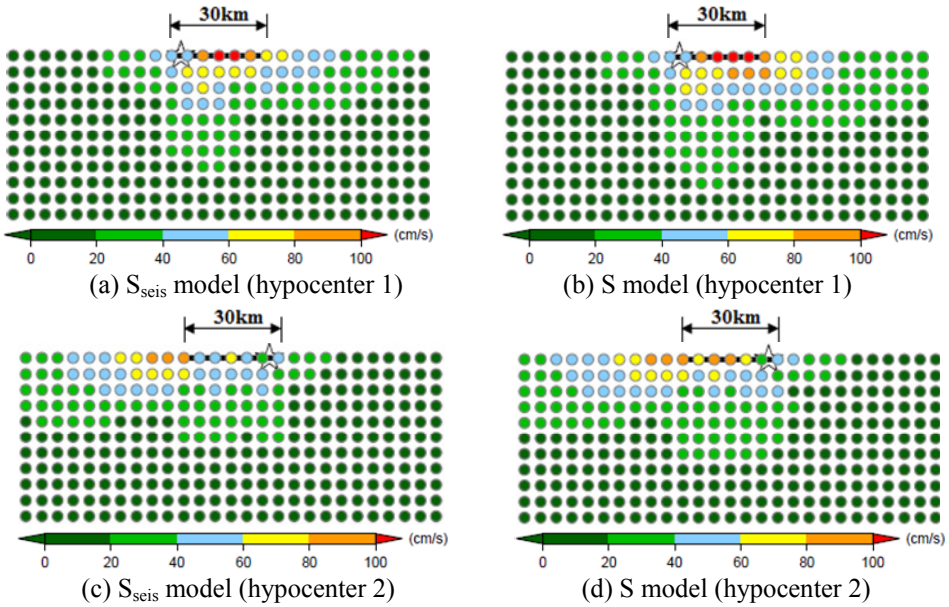

(a) S_{seis} model (hypocenter 1) (b) S model (hypocenter 1)

(c) S_{seis} model (hypocenter 2) (d) S model (hypocenter 2)

Fig. 9 Distribution of the PGV's for the 30-km long faults by the S_{seis} model and the S model. The black line is the projection of the fault model on the ground surface, and the star is the projection of the hypocenter.

4.2.4 Pseudo velocity response spectra pSv's

We calculated the geometric mean of the pseudo velocity response spectra pSv's with the damping factor of 5% at the calculation points within 10 km from the fault by the S_{seis} model and the geometric mean by the S model to compare them. Figure 11 shows the results. The number of the calculation points is 27, 39, and 65 for the 30-km, 50-km, and 200-km long faults, respectively.

It is found out that the pSv's at every period shorter than about 1 second are almost the same regardless of the S_{seis} model or the S model and the hypocenter 1 or the hypocenter 2 in each fault. On the other hand, the pSv's by the S model are 10 to 30% larger than those by the S_{seis} model in the period range longer than about 1 second in the case of the 30-km long faults shown in Fig. 11(a). Also, the pSv's by the S model are 5 to 15% larger than those by the S_{seis} model in the period range longer than about 2 seconds in the case of 50-km long faults shown in Fig. 11(b). The pSv's by the S model are slightly larger than those by the S_{seis} model in the period range longer than about 3 seconds in the case of 200-km long faults shown in Fig. 11(c). The pSv's by the S model are larger than those by the

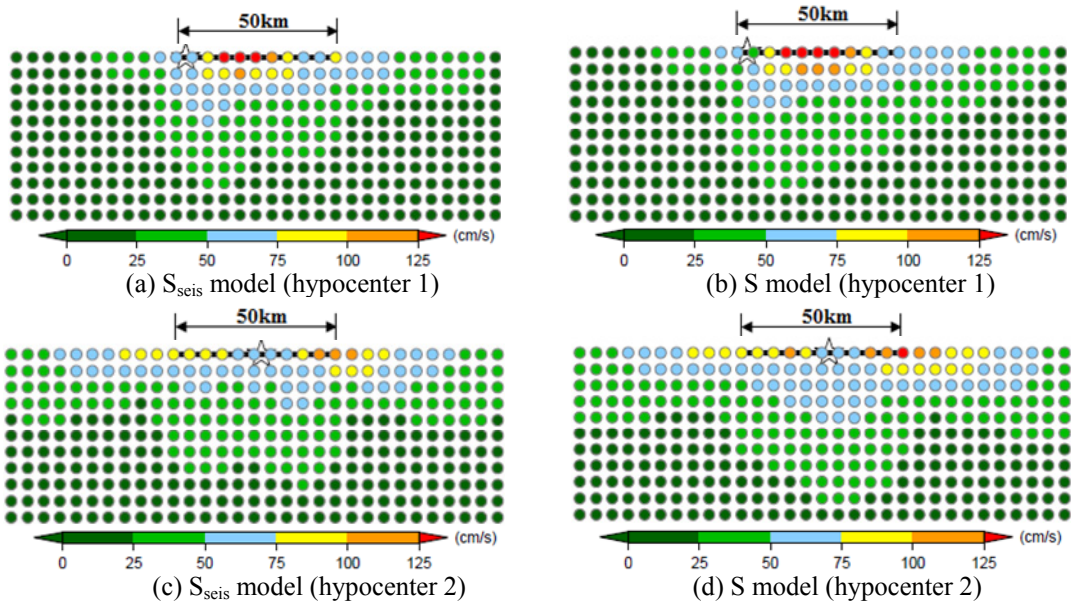

Fig. 10 Distribution of the PGV's for the 50-km long faults by the S_{seis} model and the S model. The black line is the projection of the fault model on the ground surface, and the star is the projection of the hypocenter.

S_{seis} model at longer-period range in all the cases of 30-km, 50-km, and 200-km long faults. This is because the asperity slip in the S model is larger than that in the S_{seis} model.

The pSv in the case of the hypocenter 1 is larger than that in the case of the hypocenter 2 at every period longer than about 2 seconds for the 30-km long faults and the 50-km long faults. This might be because the difference of the span of the rupture propagation in the asperity influenced the calculated motions in the area within 10 km from the fault as mentioned about the PGV's in Figs. 9 and 10.

5. CONCLUSIONS

At first, we showed the effects of the different ways of counting the fault area on the outer and inner fault parameters. The different ways of counting the fault areas were the S_{seis} model counting the seismic fault area located in the seismogenic layer and the S model counting the seismic fault area and the shallow part located in the surface layer.

The effects were that the seismic moment became 1.44 times larger, the asperity area became 1.63 times larger by adding the area of the shallow part in the second-stage earthquakes when the depth of the seismogenic layer was 3 to 18 km and that the seismic moment becomes 1.2 times larger in the third-stage earthquakes.

Next, we made vertical left-lateral strike-slip fault models for 30-km and 50-km long faults as the second-stage earthquakes and that for 200-km long fault as the third-stage earthquake, and calculated strong motions by the stochastic Green's function method. The results for the 30-km and 50-km long faults showed that the effects of the different ways of counting the fault area were small on the peak ground accelerations and that the peak ground velocities and the response spectra in the long-period range by the S model were 15 to 30% larger than those by the S_{seis} model at many calculation points. Meanwhile, the results for the 200-km long fault showed that the effects were little on the peak ground accelerations or the peak ground velocities and that the pseudo velocity response spectra by the S model in the period range longer than 3 seconds were slightly larger than those by the S_{seis} model.

We concluded that the seismic moment was underestimated and also the strong motions could be underestimated when we applied the Recipe for strong motion prediction by the Headquarters for

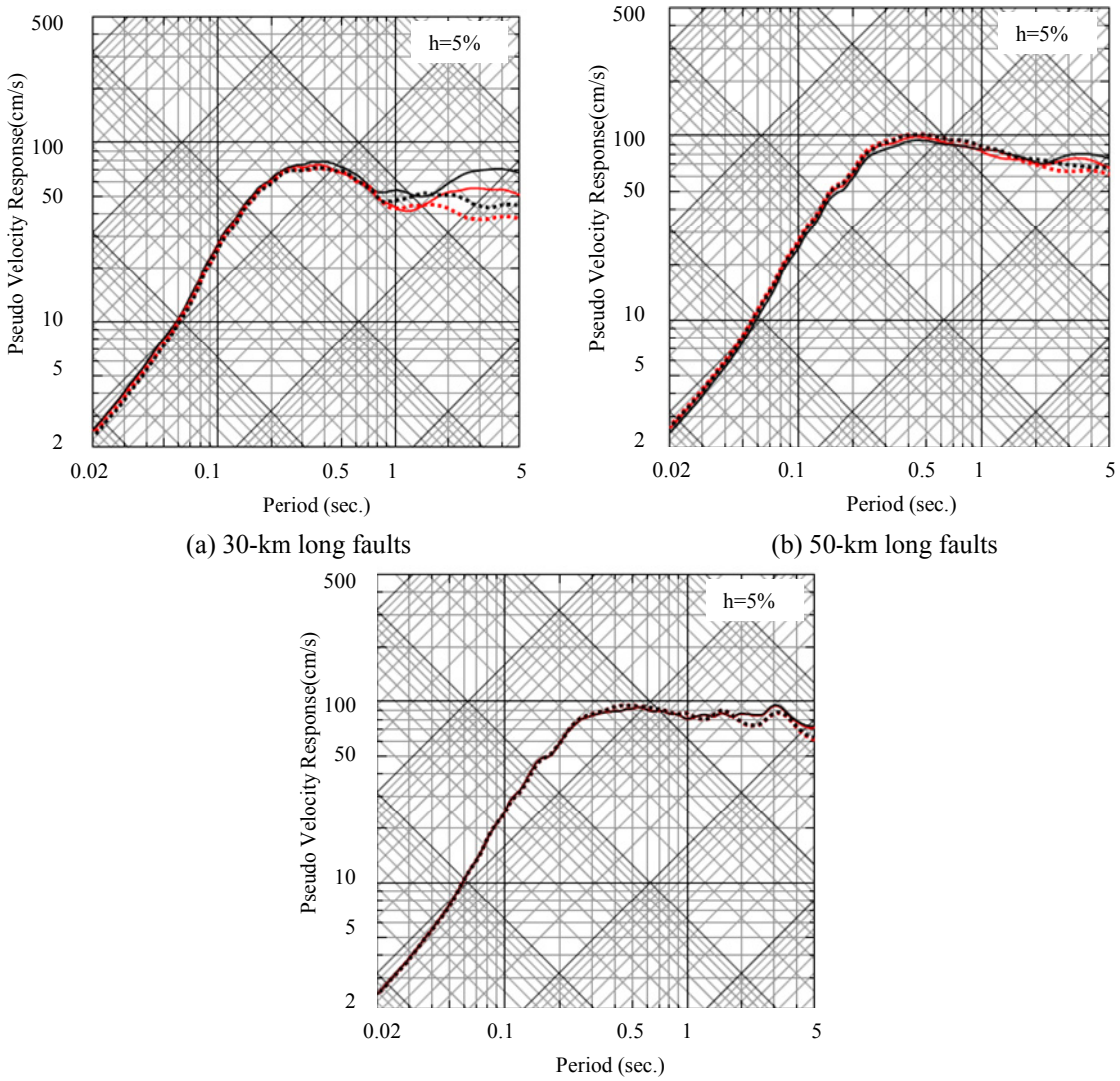

(a) 30-km long faults

(b) 50-km long faults

(c) 200-km long faults

Fig. 11 Averaged pseudo velocity response spectra at points within about 10 km from the fault. The red solid line is for the S_{seis} model with the hypocenter 1, the black solid line is for the S model with the hypocenter 1, the red dotted line is for the S_{seis} model with the hypocenter 2, and the black dotted line is for the S model with the hypocenter 2.

Earthquake Research Promotion (2016)[1] to the second-stage and the third-stage earthquakes with surface breakings.

In this paper, we assigned the entire seismic moment to the seismic fault (deep part of the fault), and calculated the strong motions. This is because we adopted the assumption in the Recipe by the Headquarters for Earthquake Research Promotion (2016)[1]. However, all the earthquakes in the second and the third stages rupture shallow parts. Hence, we have to develop a new procedure for modeling the shallow part of the fault (Ikutama *et al*., 2017[24]; Tanaka *et al*., 2017[25]) to derive the consistency with the nature.

APPENDIX: ASSIGNMENT OF THE SEISMIC MOMENT

Since the shallow part of the fault over the seismogenic layer ruptures in the second-stage and the

third-stage earthquakes, the entire seismic moment is described by

$$M_0 = \mu_{seis} S_{asp} D_{asp} + \mu_{seis} S_{back} D_{back} + \mu_{sur} S_{sur} D_{sur}. \quad \text{(A-1)}$$

Here, μ_{seis} is the rigidity at the seismic fault, S_{asp} is the asperity area, D_{asp} is the asperity slip, S_{back} is the background area, D_{back} is the background slip, μ_{sur} is the rigidity of the surface layer, S_{sur} is the area of the shallow part of the fault, and D_{sur} is the slip on the shallow part of the fault.

In equation (A-1), μ_{sur} is smaller than μ_{seis}, S_{sur} is smaller than S_{asp} and S_{back}, D_{back} is smaller than D_{asp}, and D_{sur} is almost the same as D_{asp} in the 1992 Landers earthquake and the 2016 Kumamoto earthquake, and then the term of $\mu_{sur} S_{sur} D_{sur}$ is the smallest among three terms of equation (A-1).

Actually, Irie *et al*. (2010)[15] showed that $\mu_{sur} S_{sur} D_{sur}$ was about 10% of the entire seismic moment M_0 by the dynamic fault rupturing simulation.

Hence, the entire seismic moment can be approximated by

$$M_0 \fallingdotseq \mu_{seis} S_{asp} D_{asp} + \mu_{seis} S_{back} D_{back}. \quad \text{(A-2)}$$

Although it is possible to assign the entire seismic moment M_0, calculated by the empirical relationships between the seismic moment M_0 and the entire ruptured fault area S, by using equation (A-1) we assigned the entire seismic moment to the asperity and the background by using equation (A-2) for simplicity.

Note here that it is not clear which part of the fault the seismic moment M_0 calculated from the seismic fault area S_{seis} by equation (4) or (5) should be assigned to because equations (4) and (5) were obtained from the data of the second-stage and the third-stage earthquakes, respectively, and the entire ruptured fault area S should be used to calculate the entire seismic moment.

REFERENCES

1) Headquarters for Earthquake Research Promotion: Strong ground motion prediction method for earthquakes with specified source faults ("Recipe"), 2016 (in Japanese).
2) Irikura, K. and Miyake, H.: Recipe for predicting strong ground motion from crustal earthquake scenarios, *Pure and Applied Geophysics*, Vol. 168, pp. 85-104, 2011.
3) Dan, K., Watanabe, M., Sato, T. and Ishii, T.: Short-period source spectra inferred from variable-slip rupture models and modeling of earthquake faults for strong motion prediction by semi-empirical method, *Journal of Structural and Construction Engineering* (*Transactions of the Architectural Institute of Japan*), No. 545, pp. 51-62, 2001.7 (in Japanese with English abstract).
4) Somerville, P. G., Irikura, K., Graves, R., Sawada, S., Wald, D., Abrahamson, N., Iwasaki, Y., Kagawa, T., Smith, N. and Kowada, A.: Characterizing crustal earthquake slip models for the prediction of strong ground motion, *Seismological Research Letters*, Vol. 70, No.1, pp. 59-80, 1999.
5) Irikura, K. and Miyake, H.: Prediction of strong ground motions for scenario earthquakes, *Journal of Geography*, Vol. 110, pp. 849-875, 2001 (in Japanese with English abstract).
6) Murotani, S., Matsushima, S., Azuma, T., Irikura, K. and Kitagawa, S.: Scaling relations of source parameters of earthquakes occurring on inland crustal mega-fault systems, *Pure and Applied Geophysics*, Vol. 172, pp. 1371-1381, 2015.
7) Eshelby, J. D.: The determination of the elastic field of an ellipsoidal inclusion, and related problems, *Proceedings of the Royal Society of London*, Series A, Vol. 241, pp. 376-396, 1957.
8) Madariaga, R.: On the relation between seismic moment and stress drop in the presence of stress and strength heterogeneity, *Journal of Geophysical Research*, Vol. 84, No. B5, pp. 2243-2250, 1979.
9) Brune, J. N.: Tectonic stress and the spectra of seismic shear waves from earthquakes, *Journal of Geophysical Research*, Vol. 75, No. 26, pp. 4997-5009, 1970.

10) Boatwright, J.: The seismic radiation from composite models of faulting, *Bulletin of the Seismological Society of America*, Vol. 78, No. 2, pp. 489-508, 1988.
11) Fujii, Y. and Matsu'ura, M.: Regional difference in scaling laws for large earthquakes and its tectonic implication, *Pure and Applied Geophysics*, Vol .157, pp. 2283-2302, 2000.
12) Irikura, K., Miyakoshi, K., Kamae, K., Yoshida, K., Somei, K., Kurahashi S. and Miyake, H.: Applicability of source scaling relations for crustal earthquakes to estimation of the ground motions of the 2016 Kumamoto earthquake, *Earth, Planets and Space* (2017) 69:10 DOI 10.1186/s40623-016-0586-y.
13) Wells, D. L. and Coppersmith, K. J.: New empirical relationships among magnitude, rupture length, rupture width, rupture area, and surface displacement, *Bulletin of the Seismological Society of America*, Vol. 84, No. 4, pp. 974-1002, 1994.
14) Dalguer, L. A., Irikura, K., Riera, J. and Chiu, H. C.: Fault dynamic rupture simulation of the hypocenter area of the thrust fault of the 1999 Chi-Chi (Taiwan) earthquake, *Geophysical Research Letters*, Vol. 28, No. 7, pp.1327-1330, 2001.
15) Irie, K., Dan, K., Ikutama, S. and Irikura, K.: Modeling of dynamic fault rupturing constrained by empirical relations among fault parameters of surface and subsurface faults -Toward improvement of kinematic fault model for predicting strong ground motions-, *Journal of Structural and Construction Engineering* (*Transactions of the Architectural Institute of Japan*), No. 657, pp. 1965-1974, 2010.11 (in Japanese with English abstract).
16) Geller, R. J.: Scaling relations for earthquake source parameters and magnitudes, *Bulletin of the Seismological Society of America*, Vol. 66, No.5, pp.1501-1523, 1976.
17) Dan, K., Ju, D. and Muto, T.: Modeling of subsurface fault for strong motion prediction inferred from short active fault observed on ground surface, *Journal of the Structural and Construction Engineering* (*Transactions of the Architectural Institute of Japan*), No. 648, pp. 279-288, 2010 (in Japanese with English abstract).
18) Aki, K. and Richards, P. G.: *Quantitative Seismology*, W. H. Freeman and Company, New York, 1980.
19) Boore, D. M. and Boatwright, J.: The seismic radiation from composite models of faulting, *Bulletin of the Seismological Society of America*, Vol. 74, No. 5, pp. 1615-1621, 1984.
20) Satoh, T.: Radiation pattern and f_{max} of the Tottori-ken seibu earthquake and the aftershocks inferred from Kik-net strong motion records, *Journal of Structural and Construction Engineering* (*Transactions of the Architectural Institute of Japan*), No. 556, pp. 25-34, 2002.6 (in Japanese with English abstract).
21) Tsurugi, M., Kagawa, T., Irikura, K. and Kowada, A.: Cutoff frequency f_{max} of earthquakes occurring in Kinki distinct, Programme and Abstracts, *Annual Meeting of the Seismological Society of Japan*, B41-11, 1997 (in Japanese).
22) Nozu, A.: A simple scheme to introduce near-field and intermediate-field terms in stochastic Green's functions, *Proc. 12th Japan Earthquake Engineering Symposium*, pp. 190-193, 2006 (in Japanese).
23) Miyatake, T.: Generation mechanism of strong ground motion pulse near the earthquake fault, *Journal of the Seismological Society of Japan*, Second Series, Vol. 51, pp. 161-170, 1998 (in Japanese with English abstract).
24) Ikutama, S., Kawasato, T., Kawakami, Y., Nohsho, M., Oana, A., Dan, K., Torita, H. and Okada, Y.: Source modeling for predicting ground motions and permanent displacements close to the surface fault trace, Symposium for Earthquake Ground Motion Prediction in the Near Fault Region, Japan Society of Civil Engineers, 2017 (in Japanese).
25) Tanaka, S., Kaneda, J., Hikima, K. and Hisada, Y.: Characterized fault model for prediction of long-period ground motions containing fault displacement in the near fault region, *Proc. 13th Annual Meeting of Japan Association for Earthquake Engineering*, P1-1, 2017 (in Japanese).

(Original Japanese Paper Published: August, 2018)
(English Version Submitted: December 5, 2018)
(English Version Accepted: January 15, 2019)